

Phase Diagram and Spectroscopic Evidence of Supersolids in Quantum Ising Magnet $K_2\text{Co}(\text{SeO}_3)_2$

Tong Chen^{1,11,*}, Alireza Ghasemi^{1,11}, Junyi Zhang¹, Liyu Shi¹, Zhenisbek Tagay¹, Lei Chen², Eun-Sang Choi³, Marcelo Jaime^{4,10}, Minseong Lee⁴, Yiqing Hao⁵, Huibo Cao⁵, Barry Winn⁵, Ruidan Zhong^{6,7}, Xianghan Xu⁷, N. P. Armitage¹, Robert Cava⁷, and Collin Broholm^{1,8,9,*}

¹Institute for Quantum Matter and Department of Physics and Astronomy, Johns Hopkins University, Baltimore, Maryland, USA.

²Department of Physics and Astronomy, Rice University, Houston, Texas, USA.

³National High Magnetic Field Laboratory and Department of Physics, Florida State University, Tallahassee, USA

⁴National High Magnetic Field Laboratory, Los Alamos National Laboratory, Los Alamos, New Mexico, USA.

⁵Neutron Scattering Division, Oak Ridge National Laboratory, Oak Ridge, Tennessee, USA.

⁶Tsung-Dao Lee Institute and School of Physics and Astronomy, Shanghai Jiao Tong University, Shanghai, China.

⁷Department of Chemistry, Princeton University, Princeton, New Jersey, USA.

⁸NIST Center for Neutron Research, Gaithersburg, Maryland, USA.

⁹Department of Materials Science and Engineering, Johns Hopkins University, Baltimore, Maryland, USA.

¹⁰New address: Physikalisch-Technische Bundesanstalt, Braunschweig, Germany

¹¹These authors contributed equally: Tong Chen, Alireza Ghasemi.

*e-mail: tchen115@jhu.edu, broholm@jhu.edu

ABSTRACT

A supersolid is a quantum entangled state of matter that combines features of both superfluids and solids¹⁻⁴. Despite predictions of its analog in quantum magnets⁵⁻⁸, experimental realization was lacking until recent claims in triangular-lattice compounds⁹. Here, we report the magnetic phase diagram and neutron scattering for a spin- $\frac{1}{2}$ triangular-lattice antiferromagnet, $K_2\text{Co}(\text{SeO}_3)_2$ ¹⁰. In zero field, neutron spectroscopy reveals the gradual development of a $\sqrt{3} \times \sqrt{3}$ magnetic order associated with Z_3 symmetry breaking for temperatures $5 \text{ K} < T < 15 \text{ K}$. Below 5 K, the emergence of a Goldstone mode from low-energy continuum scattering suggests that the system enters a supersolid phase characterized by the breaking of both Z_3 and spin rotational $U(1)$ symmetry. In c -axis-oriented magnetic fields $1.1 \text{ T} < B < 21 \text{ T}$, a prominent $\frac{1}{3}$ magnetization plateau phase emerges, accompanied by a distinct high-field supersolid phase ($18 \text{ T} < B < 21 \text{ T}$). From the coherent spin wave excitations in the $\frac{1}{3}$ magnetized plateau phase, we infer the spin Hamiltonian, which features nearest neighbor interactions with $J_z = 2.98(2) \text{ meV}$ and $J_\perp = 0.21(3) \text{ meV}$. Our work demonstrates that $K_2\text{Co}(\text{SeO}_3)_2$ is a spectacular example of a spin- $\frac{1}{2}$ triangular-lattice quantum Ising antiferromagnet, documents its magnetic phase diagram highlighting two supersolid phases, and provides spectroscopic evidence of zero-field supersolidity.

Introduction

While the coexistence of superfluidity and solidity may appear counterintuitive, at the microscopic level, supersolids are characterized by the spontaneous breaking of both $U(1)$ gauge symmetry (superfluid) and translational symmetry (solid)¹⁻⁴. Starting from solid ^4He ¹¹⁻¹⁵, the prediction of supersolidity has been extended to various systems of ultracold gases¹⁶⁻¹⁹, as well as triangular lattices of hard-core bosons²⁰⁻²⁴. When considering the mapping of hard-core bosons onto spin- $\frac{1}{2}$ degrees of freedom (see Methods), it is natural to ask whether supersolidity exists in spin- $\frac{1}{2}$ triangular-lattice quantum magnets. The corresponding Hamiltonian is described by:

$$\mathcal{H} = \sum_{\langle i,j \rangle} [J_z S_i^z S_j^z + J_\perp (S_i^x S_j^x + S_i^y S_j^y)] - g_z \mu_B B_z \sum_i S_i^z \quad (1)$$

where the first sum is over adjacent sites, $J_z > 0$ and $J_\perp > 0$ are antiferromagnetic Ising and transverse exchange constants, S_k^α is a spin- S operator, and the second sum is the Zeeman term which describes the effect of an external field $B_z \parallel \hat{z}$.

Exploring supersolidity in this model with easy-axis exchange ($J_\perp < J_z$) presents both experimental and theoretical

challenges, including the scarcity of suitable experimental model systems and the notorious sign problem in the quantum Monte Carlo (MC) technique. In 2009, the density matrix renormalization group (DMRG)⁵ and variational MC⁶ analysis uncovered the $\sqrt{3} \times \sqrt{3}$ supersolid ground state for all $J_{\perp} < J_z$. In 2014, the cluster mean-field⁷ and DMRG⁸ methods succeeded in unraveling the phase diagrams and discovered a second supersolid phase in c-axis-oriented magnetic fields.

Recently, the layered triangular-lattice compound $\text{K}_2\text{Co}(\text{SeO}_3)_2$, hereafter referred to as KCSO, was proposed to be a triangular-lattice antiferromagnet with a significant easy-axis exchange anisotropy¹⁰. While magnetic susceptibility measurements indicate anisotropic antiferromagnetic interactions ($\Theta_{\text{CW},\perp} = -209$ K, $\Theta_{\text{CW},\parallel} = -7.0$ K), there is no sharp thermal anomaly in the zero-field specific heat capacity $C_p(T)$, indicating low dimensional and/or geometrically frustrated magnetism. Here, we investigate KCSO through heat capacity, magnetization, and neutron scattering experiments. We find that KCSO is a spin- $\frac{1}{2}$ 2D triangular-lattice antiferromagnet near the Ising limit (hereafter referred to as a quantum Ising magnet), and we determine the spin-Hamiltonian (Eq. 1). In zero field, we report the gradual development of a quasi-2D $\sqrt{3} \times \sqrt{3}$ magnetic order and a low-energy continuum of excitations within the temperature range of 5 K to 15 K. Below 5 K, an increase in the correlation length and the emergence of a Goldstone mode indicate U(1) rotational symmetry breaking consistent with a supersolid phase. In mapping the field-temperature phase diagram, we document a phase transition of the three-state Potts model universality class to a $\frac{1}{3}$ magnetization plateau phase for fields above 1.1 T and provide experimental evidence for a distinct high-field phase that was previously predicted to be a supersolid.

Magnetic Order

We first investigate the magnetic order of KCSO using elastic neutron scattering (see Methods). Figures 1f-h show magnetic elastic scattering at 0.1 K in the $(hk0)$, (hhl) , and $(k\bar{k}l)$ planes under 0 T and 7 T magnetic fields applied along the c-axis. A 12 K data set was subtracted as background. In zero field, despite the absence of sharp peaks in $C_p(T)$ data, elastic scattering sharply concentrates at $(\frac{1}{3}\frac{1}{3})$, the K points, of the 2D Brillouin zone (Fig. 1f) and exhibits a rod-like character in the (hhl) plane (Fig. 1g). This indicates a quasi-2D $\sqrt{3} \times \sqrt{3}$ magnetic order. The absence of rod scattering at the Γ points indicates that the dipole moment of each layer vanishes within the correlation volume defined by the $(\frac{1}{3}\frac{1}{3})$ rod. In a 7 T field, the $(\frac{1}{3}\frac{1}{3})$ rod-like scattering is enhanced, and 3D Bragg peaks develop at Γ points (Fig. 1f,h). The combination of magnetic Bragg diffraction on top of nuclear Bragg peaks and K-point rod scattering indicates field-induced quasi-2D Up-Up-Down (UUD) order (Fig. 1b).

Figures 1i,j show the magnetic elastic scattering along the (hh) and l directions for 0 T and 7 T magnetic fields. The light blue open circles represent magnetic scattering measured at 5 K without final energy resolution on the HB-3A neutron diffractometer. The broad peak versus l indicates quasi-2D magnetic order with moments oriented along the c-axis. Solid and dashed lines are fits to the following formula²⁵ with $(\alpha_n \neq 0)$ and without $(\alpha_n = 0)$ inter-plane correlations respectively and with $m_{\perp} = 0$:

$$I(\mathbf{Q}) = N_M \frac{(2\pi)^2}{A_M} \left(\frac{\gamma r_0}{2} \right)^2 |F(\mathbf{Q})|^2 \times (1 + 2\sum_n \alpha_n \cos(2\pi l \frac{n}{3})) \times \left(m_z^2 (1 - \hat{Q}_z^2) |\mathcal{F}_{\parallel}(\mathbf{Q})|^2 + \frac{1}{2} m_{\perp}^2 (1 + \hat{Q}_z^2) |\mathcal{F}_{\perp}(\mathbf{Q})|^2 \right). \quad (2)$$

Here N_M and A_M are the number and in-plane area of magnetic unit cells, $\gamma r_0 = -0.54 \cdot 10^{-12}$ cm is the magnetic scattering length, \mathbf{Q} is the momentum transfer, $F(\mathbf{Q})$ is the Co^{2+} magnetic form factor²⁶, $(1 + 2\sum_n \alpha_n \cos(2\pi l \frac{n}{3}))$ accounts for correlations between n^{th} nearest neighboring planes, and $\mathcal{F}_{\parallel,\perp}(\mathbf{Q}) = \sum_j \text{sgn}(m_{j\parallel,\perp}) \exp(i\mathbf{Q} \cdot \mathbf{d}_j)$ is the scalar magnetic structure factor for spins at locations \mathbf{d}_j within the $\sqrt{3} \times \sqrt{3}$ magnetic unit cell. $(1 - \hat{Q}_z^2)$ and $(1 + \hat{Q}_z^2)$ are polarization factors for the squared out-of-plane dipole moment m_z^2 and the domain averaged squared in-plane moment $\frac{1}{2} m_{\perp}^2$, respectively.

In an applied field, the magnetization data in Figures 2a and 3b reveal an extended $\frac{1}{3}$ magnetization plateau, consistent with a quasi-2D UUD phase. While the uniform magnetization is reflected in the appearance of magnetic Bragg diffraction at the $(0, 1, \pm 1)$ Γ -points, the weakly l -dependent scattering at $(\frac{1}{3}\frac{1}{3})$ indicates a 2D phase with short-range correlations along c. Equation 2 provides an excellent account of the data with $\alpha_{3-6} = (-0.002(8), 0.00(2), 0.02(2), -0.002(9))$ indicating weak ferromagnetic correlations between unit cells. Since the data only cover the range $|l| \leq 0.7$ with the Q_z resolution given by the horizontal bar in Figure 1j, they are only sensitive to correlations between $3 \leq n \leq 6$ neighboring planes. For consistency with the magnetization data, we normalize the diffraction data to the saturation magnetization $m_z = 3.90 \mu_B/\text{Co}$ in Equation 2.

At 5 K in zero field, two possible collinear quasi-2D orders²⁷⁻²⁹, $U_{/2}U_{/2}D$ (Fig. 1c) and UD0 (Fig. 1d), both produce $(\frac{1}{3}\frac{1}{3})$ magnetic diffraction with squared structure factors $|\mathcal{F}_{\parallel}(\frac{1}{3}\frac{1}{3})|^2$ equal to 9/4 and 3, respectively. Because no modulation beyond that associated with the polarization factor is observed in the data, we infer $\alpha_n \approx 0$ and obtain a limit on the in-plane component of the staggered magnetization: $m_{\perp} \leq 0.3 \mu_B$. The out-of-plane ordered moment inferred is $m_z = 2.51(2) \mu_B/\text{Co}$ for $U_{/2}U_{/2}D$ order versus $m_z = 2.18(2) \mu_B/\text{Co}$ for UD0 order.

At 0.1 K in zero field, the $(\frac{1}{3}\frac{1}{3}l)$ scan displays two peaks at $l = \pm 0.5$ (Fig. 1g,j), indicating antiferromagnetic correlations between planes separated by c. Fitting the l dependence to Equation 2 yields $m_z = 3.09(3) \mu_B/\text{Co}$ and $\alpha_{3-6} =$

($-0.08(2), 0.03(3), 0.03(3), -0.02(2)$). While all numerical methods including classical/variational MC^{6,27–29}, cluster mean-field⁷, and DMRG^{5,8} analysis predicted the supersolid “Y” state (Fig. 1a) featuring an in-plane moment m_{\perp} , the range of the scan is insufficient to experimentally distinguish inter-plane correlations from the effect of m_{\perp} .

The integrated intensity and in-plane correlation length, ξ , of the magnetic diffraction at $(\frac{1}{3}, \frac{1}{3}, |l| \leq 0.4)$ obtained from neutron scattering with $|\hbar\omega| \leq 0.1$ meV are shown as functions of temperature in zero field in Figure 1e (See Supplementary Information for details). For temperatures $5 \text{ K} < T < 15 \text{ K}$, the integrated intensity increases upon cooling as the magnitude of the quasi-static staggered magnetization increases. Below 5 K, the in-plane correlation length increases precipitously toward the resolution limit while the integrated intensity decreases significantly. Both antiferromagnetic inter-plane correlations and in-plane moment m_{\perp} shift intensity from $l = 0$ to finite l that was not covered in the integration, resulting in a drop in the integrated intensity. Based on the thermodynamic data and the inelastic neutron scattering in the following, we attribute the increase in correlation length and decrease in integrated intensity to the emergence of supersolidity.

Phase Diagram

We now explore the field-temperature phase diagram for KCSO in c-oriented magnetic fields. The uniform magnetization, M , and differential susceptibility, dM/dT , data for fields up to 30 T are shown in Figures 2a and 2c, respectively (see Methods for details). Upon cooling in fields between 2 T and 18 T, the magnetization approaches $1/3$ of the $3.90 \mu_{\text{B}}/\text{Co}$ saturation magnetization. In fields beyond 22 T, the magnetization tends to the saturation magnetization at low temperatures. The field-temperature phase diagram indicated by dM/dT (Fig. 2c) is consistent with theoretical analysis of the classical antiferromagnetic Ising model on the triangular lattice with $J_z \approx 2.96 \text{ meV}$ ^{30–33}.

For fields between 18 T to 20 T, an additional phase becomes apparent in the double peak structure of dM/dT versus temperature. This observation aligns with cluster mean-field and DMRG studies of the model described by Equation 1 with the transverse component $J_{\perp} \ll J_z$ ^{7,8}. Comparing the $T \rightarrow 0$ phase boundaries with calculated phase diagrams suggests $J_{\perp} \approx 0.27 \text{ meV}$. J_z and J_{\perp} will be precisely determined from coherent spin wave excitations in the next section. Despite different spin configurations, this high-field supersolid phase is also expected to break both Z_3 and $U(1)$ symmetries as the zero-field supersolid phase^{7,8}.

Figure 2b shows the specific heat capacity, C_p , of KCSO versus temperatures for magnetic fields below 14 T. In zero field, the specific heat exhibits a broad peak centered around 1.0 K, while at higher fields, a distinct sharp anomaly indicating a second-order phase transition emerges. The sharp peak becomes more pronounced and shifts to higher temperatures with increasing fields, eventually reaching a maximum temperature of 11.4 K for $B = 10 \text{ T}$. These data extend previous results¹⁰, and the phase boundary above 2 T is consistent with that determined from dM/dT versus temperature (Fig. 2c). In c-axis-oriented fields, the phase boundary of the UUD and paramagnetic phases are associated with Z_3 symmetry breaking and are predicted to be in the 2D three-state Potts universality class for both classical³⁴ and quantum Ising models on triangular lattices^{7,8}. Critical exponent fitting of C_p versus temperature yields $\alpha = 0.318(3)$ (see Supplementary Information for details). This confirms our interpretation of the phase transition to the UUD phase since $\alpha = 1/3$ for the three-state Potts model on a 2D lattice³⁵.

To explore the low-field and low-temperature region of the phase diagram, we investigate the magnetic field dependence of M , dM/dB , and C_p in Figure 3. The $B \rightarrow 0$ differential susceptibility dM/dB continues to increase upon cooling to the lowest temperatures accessed (0.3 K), indicating that the magnetic excitation spectrum remains gapless at low fields. Indeed, at the lowest B and T , dM/dB increases with the field, leading to a peak at an apparent crossover field that approaches $B \approx 0.51(3) \text{ T}$ at low T . Considering that Z_3 symmetry is broken in the UUD phase, the fact that this phase can be accessed through a crossover at the lowest temperature indicates that Z_3 symmetry is effectively broken in zero field at these temperatures, as also apparent from the diverging correlation length (Fig. 1e). We may associate the crossover with gradually suppressing the transverse part of the quasi-static moment i.e. closing the “Y” to form the UUD state.

At 5 K where the transverse component of the magnetic order is absent (Fig. 1j light blue open circles), so is the crossover peak in dM/dB . Instead, M is proportional to B at low fields (Fig. 3a) and dM/dB remains constant (Fig. 3b). At these temperatures the transition to the UUD phase is marked by a sharp peak that is associated with the Potts transition to the UUD phase. The specific heat capacity data in Figures 3d,e show the appearance of a distinct second-order phase transition peak on top of a broad maximum for $T > 4 \text{ K}$. If this is an actual critical endpoint for the Potts transition, an unseen Berezinskii–Kosterlitz–Thouless (BKT) transition lines associated with the Z_3 symmetry might extend to zero field from this point. Further experimental work in this regime is needed to explore the theoretical prediction of two successive BKT transitions associated with Z_3 and $U(1)$ symmetry breaking, respectively^{27–29}.

At higher temperatures, the Potts transition peak gains strength (Fig. 3c) and shifts to higher fields with increasing temperature, until at 10 K, the reentrant nature of the UUD phase becomes apparent as a second sharp peak associated with the upper boundary of the UUD phase is observed within the accessible 14 T field range. However, the additional phase reminiscent of “supersolid”, identified in dM/dT (Fig. 2c), is not apparent in this high-temperature regime.

Coherent Spinwaves in the UUD Phase

Figure 4a presents the inelastic magnetic neutron scattering cross-section versus energy and momentum along high-symmetry directions acquired in a 7 T magnetic field. The data reveal three coherent spin-wave modes of excitation, as anticipated for a long-range ordered $\sqrt{3} \times \sqrt{3}$ UUD structure. The absence of measurable dispersion along the c-axis indicates a highly 2D spin system, as also evident from the rod-like magnetic diffraction data (Fig. 1f). We associate the highest energy excitation with flipping a D spin, all of which are surrounded by $z = 6$ U spins in the UUD phase. Spin-wave propagation is driven by the transverse exchange, which can reverse an anti-parallel spin pair. However, since the reversed D spin is surrounded by U spins, no such propagation is possible, resulting in a dispersionless mode. The energy cost of the spin flip is approximately $2zJ_z(\frac{1}{2})^2 - g_z\mu_B B \approx 5.72$ meV, consistent with Figure 4a. Here, we used $J_z \approx 2.96$ meV and $g_z = 7.8$, inferred from the field-temperature phase diagram and the saturation magnetization, respectively.

The two lower energy dispersive modes are associated with flipping each of the two U spins per unit cell. Since U spins are surrounded by an equal number of U and D spins, the \mathbf{Q} -averaged energy for these modes is simply $g_z\mu_B B_z = 3.16$ meV. The presence of dispersion for these modes is a consequence of the newly minted D site having (three) U sites to move onto through the transverse exchange term. The bandwidth provides an estimate for $3J_\perp \approx 0.81$ meV, which is consistent with Figure 4a.

For a detailed quantitative test of spin-wave theory as a means of describing the data, a pixel-to-pixel least squares fit of the data in Figure 4a was conducted. Here, the singular spin-wave cross section was convoluted with a Gaussian energy resolution with the average full-width half-maximum energy resolution of 0.2 meV. The weak dispersion allows us to neglect the finite \mathbf{Q} -resolution of the instrument. An excellent account of the data is obtained with $J_z = 2.98(2)$ meV and $J_\perp = 0.21(3)$ meV as shown in Figure 4b. By admitting the next-nearest-neighbor interactions, we obtain tight constraints on these: $J_z^{(2)} = 0.02(1)$ meV and $J_\perp^{(2)} = 0.01(1)$ meV. This is important to know as ferromagnetic (antiferromagnetic) interactions between next-nearest neighbors within the plane stabilize $U/2U/2D$ (UD0) ground state³⁶. Apart from quantitatively establishing the spin-Hamiltonian for KCSO, Figure 4 and the associated analysis provide evidence for the high quality of the multi-crystal sample, which will be relevant in the following.

Magnetic Excitations in Zero Field

We now explore the low-temperature magnetic excitations in zero field. Here, we observe $\sqrt{3} \times \sqrt{3}$ quasi-static spin correlations with a correlation length exceeding $\xi > 200 a$ and less than 80% of the sublattice magnetization observed in the UUD phase at 7 T. Figure 5a shows the energy- and momentum-dependence of inelastic magnetic scattering at 0.1 K (From HYSPEC with $E_i = 9.0$ meV). The data contain three bands of magnetic scattering near 0 meV, 3 meV, and 6 meV, which exhibit some structure and are broader than the energy resolution (Fig. 5a-c). The broad, \mathbf{Q} -dependent scattering (Fig. 5b,c) is most intense near the boundaries of the Brillouin zone and resembles a dimer structure factor for spin pairs separated by $\langle 100 \rangle$.

To understand these features, we consider a quantum Ising magnet in the limit $J_\perp/J_z \rightarrow 0$ ($J_\perp/J_z = 0.070$ for KCSO). In this picture, magnetic excitations take the form of individual spin flips with energies given by $\hbar\omega = J_z \sum_i S_i^z - g_z\mu_B B_z$, where the summation is over nearest neighbors. For KCSO where each spin has six nearest neighbors, we can expect excitations at $\hbar\omega_n = nJ_z$, where $n = 0, 1, 2, 3$. Considering the value of $J_z = 2.98$ meV, this accounts for the three bands observed in the energy range covered. The highest energy band at $\hbar\omega_3$ was confirmed with THz spectroscopy (see methods). At 5 K, the lowest energy band of excitation at $\hbar\omega_0$ increases linearly in energy with the magnetic field, while the highest energy band at $\hbar\omega_3$ decreases linearly. These bands become spin-wave excitations in the UUD phase (see details in Supplementary Information).

The \mathbf{Q} -dependence of the scattering in each band (Fig. 5b,c,e,f) distinguishes KCSO from the simple Ising picture and is evidence of quantum dynamics induced by the finite value of $J_\perp = 0.21$ meV. In the higher energy bands, the wave vector dependence of the scattering reflects the momentum space wave function of a spin flip. The zone boundary nature of the scattering indicates antiferromagnetic correlations between nearest neighbors in the excited state³⁷.

Figure 5d-f show that the lowest energy band of scattering at $\hbar\omega_0$ takes the form of a dispersive low-energy continuum centered on the Brillouin zone boundary with most intensity at the ordering wave vector, K. Consistent with the specific heat capacity (Fig. 3e) and magnetization data (Fig. 3b), the spectrum appears to be gapless at K and has a small gap < 0.1 meV at the M point. Dispersion is apparent at M and K both in the E - \mathbf{Q} slice (Fig. 5d) and in Figures 5e,f, which show loss of intensity at K for $\hbar\omega > 0.3$ meV, resembling a collective Goldstone mode. However, all of these features are not resolution-limited but rather resemble the two-spinon scattering cross-section for spin-1/2 chain materials³⁸⁻⁴¹. The contrast between these data and those from the UUD plateau phase, which are dominated by coherent spin waves, suggests that a description of the low-energy excitations as a two-particle continuum scattering may be appropriate.

Summary and Conclusions

$\text{K}_2\text{Co}(\text{SeO}_3)_2$ turns out to be a great material in which to explore the quantum collective properties of a foundational model in frustrated magnetism: the spin-1/2 triangular lattice Ising model with weak transverse exchange interactions. The 1/3 plateau phase, which has long-range UUD three sublattice order is accessible to inelastic neutron scattering through which we find coherent spin wave modes that can be described by Equation 1 with $J_z = 2.98(1)$ meV and $J_\perp = 0.21(3)$ meV. In particular, the absence of dispersion of the minority spin-flip excitation is direct experimental evidence that nearest neighbor interactions are dominant ($J_{\perp,z}^{(2)} \leq 0.02$ meV). The ratio $J_z/J_\perp = 14(1)$ places KCSO deeply in the Ising limit though with quantum dynamics that can readily be exposed with modern neutron scattering instrumentation.

We have been able to map the entire $B - T$ phase diagram and characterize the static and dynamic properties of the lower field phases. A high field phase that is consistent with theoretical predictions of a supersolid is currently inaccessible to inelastic neutron scattering. While the gapless nature of the zero field state is apparent from specific heat capacity and magnetization data, our inelastic neutron scattering data show the gap only closes at the $(\frac{1}{3}, \frac{1}{3})$ K point indicating that the gapless spectrum arises through the Goldstone mechanism due to the long length scale breaking of a continuous degree of freedom. This is spectroscopic evidence that a continuous degree of freedom, the U(1) spin rotation symmetry about the c-axis has been broken on a long length scale. Therefore, through the mapping between the spin model and a model of hard-core bosons on the triangular lattice, the coexistence of the Goldstone mode (breaking the U(1) symmetry) and the $\sqrt{3} \times \sqrt{3}$ order (breaking the translational symmetry) implies a supersolid state in which a superfluid of bosons also has solid-like spatial modulations.

In the course of finalizing the paper, a preprint appeared on ArXiv reporting neutron scattering experiments on KCSO⁴². The experimental data are consistent with those reported here. However, it only covers the lower energy range, so that a complete model could not be developed.

Methods

Hard-Core Boson Representation

To understand the quantum magnetic order emerging in systems of spin-1/2 on triangular lattices described by Hamiltonian of Equation(1), it is convenient to represent the spin operators with hard-core bosons

$$S_i^z = n_i - \frac{1}{2}, \quad S_i^+ = b_i^\dagger, \quad S_i^- = b_i, \quad (3)$$

where $n_i = b_i^\dagger b_i$ is restricted to 0 or 1.

The Hamiltonian (Eq.(1)) represented in terms of the hard-core bosons becomes

$$\mathcal{H} = \sum_{\langle i,j \rangle} \left[V \left(n_i - \frac{1}{2} \right) \left(n_j - \frac{1}{2} \right) - t (b_i^\dagger b_j + b_j^\dagger b_i) \right] - \mu \sum_i \left(n_i - \frac{1}{2} \right), \quad (4)$$

where the model parameters $V = J_z$, $-t = \frac{J_\perp}{2}$ and $\mu = g\mu_B B_z$. In this bosonic representation, $V > 0$ signifies a repulsive interaction between nearest neighbor bosons, $-t$ is the hopping amplitude, and μ stands for the chemical potential. The rotational symmetry of x, y components of the spins becomes U(1)-symmetry of the bosons.

Our primary focus lies on two distinct types of orders: 1) the diagonal charge order, and 2) the off-diagonal phase order. The diagonal charge order manifests as charge density waves (or equivalently, spatial modulations in S^z), which is often referred to as solid phase. The off-diagonal order involves the spontaneous breaking of the U(1) symmetry, which is often referred to as the superfluid phase. The Mermin-Wagner theorem dictates that no true long-range orders associated with a continuous symmetry that is spontaneously broken can develop at finite temperatures. Instead, in the superfluid phase only quasi-long range order prevails at low temperatures, while the proliferation of the vortices, as per the BKT mechanism, destroys coherence at high temperatures.

It has been suggested that the antiferromagnetic Heisenberg model on triangular lattices with easy-axis anisotropy can host phases bearing both diagonal and off-diagonal long-range orders, which are also known as supersolids.

Materials Synthesis

$\text{K}_2\text{Co}(\text{SeO}_3)_2$ single crystals were synthesized using a previously described solid-state reaction method¹⁰ at Johns Hopkins University and Princeton University. X-ray diffraction analysis of polycrystalline samples revealed the absence of stacking faults or secondary phases. The crystals were found to crystallize in space group $R\bar{3}m$ (No. 166), with lattice constants $a = b = 5.5049(7)$ Å, and $c = 18.411(3)$ Å at 100 K.

Specific Heat

The specific heat capacity of KCSO was measured using a thermal-relaxation method in a Quantum Design Physical Properties Measurement System (PPMS) at Johns Hopkins University. A 2.1 mg plate-like sample was mounted horizontally so that the c -axis was oriented along the vertical field direction of the 14 T magnet.

Magnetization

The high-field magnetization data were obtained using a conventional vibrating sample magnetometer (VSM) and a water-cooled resistive magnet in Cell 8 of the DC Field Facility of the National High Magnetic Field Laboratory (NHMFL) in Tallahassee, FL. The VSM was calibrated using a standard Ni sphere and the sample was glued to a polycarbonate sample holder with GE7031 varnish. These magnetization data were normalized by comparison to a DC-magnetization measurement with a VSM in a 14 T PPMS (Quantum Design) at Johns Hopkins University.

The magnetization in millisecond pulsed magnets reaching up to 60 T was measured at the NHMFL pulsed field facility at Los Alamos National Laboratory. The experiments were conducted in three configurations with magnetic fields along the c -axis, the zigzag, and the armchair directions in the ab -plane. To reduce the background from the spatially uniform pulsed magnetic field, the samples were placed in a radially counter-wound copper coil. An additional one turn of the coil further compensated for any residual signals. For each magnetization cure, two configurations, with the sample inside and outside the coil, were measured at the same temperature, and the sample-out curve was subtracted from the sample-in curve. The temperature was stabilized using a ^3He and ^4He dilution refrigerator. A Lakeshore Cernox thermometer recorded the temperatures before each field pulse.

Neutron Scattering

Neutron diffraction data of KCSO were acquired using the HB-3A DEMAND⁴³ at the High Flux Isotope Reactor at Oak Ridge National Laboratory. An 8.22 mg single crystal was mounted on an aluminum holder and cooled in a cryostat with a base temperature of 5 K. The experiment used the four-circle mode and a beam of neutrons with wavelength $\lambda = 1.542$ Å wavelength from a bent Si-220 monochromator.

The inelastic neutron scattering data were acquired on the HYSPEC spectrometer at Oak Ridge National Laboratory. A total of 0.9 g of single crystals were co-aligned for scattering in the $(hk0)$ reciprocal lattice plane on an aluminum mount and installed in a dilution refrigerator, with a base temperature of 70 mK and an 8 T vertical field magnet. In the 0.1 K 0 T measurement, a 0.02 T field was applied to suppress the superconductivity of the sample mount. Incident energies $E_i = 3.8$ meV and 9.0 meV with a 240 Hz chopper frequency. The sample was rotated by 60° or 120° in 2° steps. The inelastic neutron scattering data were normalized using the incoherent scattering cross-section for KCSO.

THz spectroscopy

Time domain terahertz spectroscopy measurements were performed in a home-built system equipped with a commercial fiber-coupled Toptica spectrometer and a 6.5 T superconducting magnet⁴⁴. The magnetic field was applied perpendicular to the plane ($B \parallel c$). The complex THz transmission matrix was measured in a frequency range of 0.2 THz to 2 THz.

References

1. Thouless, D. The flow of a dense superfluid. *Annals Phys.* **52**, 403–427 (1969).
2. Andreev, A. & Lifshits, I. Quantum theory of defects in crystals. *Zhur Eksper Teoret Fiziki* **56**, 2057–2068 (1969).
3. Chester, G. Speculations on bose-einstein condensation and quantum crystals. *Phys. Rev. A* **2**, 256 (1970).
4. Leggett, A. J. Can a solid be "superfluid"? *Phys. Rev. Lett.* **25**, 1543 (1970).
5. Jiang, H., Weng, M., Weng, Z., Sheng, D. & Balents, L. Supersolid order of frustrated hard-core bosons in a triangular lattice system. *Phys. Rev. B* **79**, 020409 (2009).
6. Heidarian, D. & Paramakanti, A. Supersolidity in the triangular lattice spin-1/2 XXZ model: A variational perspective. *Phys. review letters* **104**, 015301 (2010).
7. Yamamoto, D., Marmorini, G. & Danshita, I. Quantum phase diagram of the triangular-lattice XXZ model in a magnetic field. *Phys. Rev. Lett.* **112**, 127203 (2014).
8. Sellmann, D., Zhang, X.-F., Eggert, S. *et al.* Phase diagram of the antiferromagnetic XXZ model on the triangular lattice. *Phys. Rev. B* **91**, 081104 (2015).
9. Xiang, J. *et al.* Giant magnetocaloric effect in spin supersolid candidate $\text{Na}_2\text{BaCo}(\text{PO}_4)_2$. *Nature* **625**, 270–275 (2024).

10. Zhong, R., Guo, S. & Cava, R. Frustrated magnetism in the layered triangular lattice materials $\text{K}_2\text{Co}(\text{SeO}_3)_2$ and $\text{Rb}_2\text{Co}(\text{SeO}_3)_2$. *Phys. Rev. Mater.* **4**, 084406 (2020).
11. Kim, E. & Chan, M. H.-W. Probable observation of a supersolid helium phase. *Nature* **427**, 225–227 (2004).
12. Balibar, S. The enigma of supersolidity. *Nature* **464**, 176–182 (2010).
13. Kim, D. Y. & Chan, M. H. Absence of supersolidity in solid helium in porous vycor glass. *Phys. Rev. Lett.* **109**, 155301 (2012).
14. Boninsegni, M. & Prokof'ev, N. V. Colloquium: Supersolids: What and where are they? *Rev. Mod. Phys.* **84**, 759 (2012).
15. Nyéki, J. *et al.* Intertwined superfluid and density wave order in two-dimensional ^4He . *Nat. Phys.* **13**, 455–459 (2017).
16. Li, J.-R. *et al.* A stripe phase with supersolid properties in spin–orbit-coupled bose-einstein condensates. *Nature* **543**, 91–94 (2017).
17. Léonard, J., Morales, A., Zupancic, P., Esslinger, T. & Donner, T. Supersolid formation in a quantum gas breaking a continuous translational symmetry. *Nature* **543**, 87–90 (2017).
18. Tanzi, L. *et al.* Supersolid symmetry breaking from compressional oscillations in a dipolar quantum gas. *Nature* **574**, 382–385 (2019).
19. Norcia, M. A. *et al.* Two-dimensional supersolidity in a dipolar quantum gas. *Nature* **596**, 357–361 (2021).
20. Melko, R. *et al.* Supersolid order from disorder: Hard-core bosons on the triangular lattice. *Phys. review letters* **95**, 127207 (2005).
21. Wessel, S. & Troyer, M. Supersolid hard-core bosons on the triangular lattice. *Phys. review letters* **95**, 127205 (2005).
22. Boninsegni, M. & Prokof'ev, N. Supersolid phase of hard-core bosons on a triangular lattice. *Phys. review letters* **95**, 237204 (2005).
23. Heidarian, D. & Damle, K. Persistent supersolid phase of hard-core bosons on the triangular lattice. *Phys. review letters* **95**, 127206 (2005).
24. Wang, F., Pollmann, F. & Vishwanath, A. Extended supersolid phase of frustrated hard-core bosons on a triangular lattice. *Phys. Rev. Lett.* **102**, 017203 (2009).
25. Stock, C. *et al.* Neutron-scattering measurement of incommensurate short-range order in single crystals of the $s=1$ triangular antiferromagnet NiGa_2S_4 . *Phys. review letters* **105**, 037402 (2010).
26. Clementi, E. & Roetti, C. Roothaan-hartree-fock atomic wavefunctions: Basis functions and their coefficients for ground and certain excited states of neutral and ionized atoms, $Z \leq 54$. *At. data nuclear data tables* **14**, 177–478 (1974).
27. Miyashita, S. & Kawamura, H. Phase transitions of anisotropic heisenberg antiferromagnets on the triangular lattice. *J. Phys. Soc. Jpn.* **54**, 3385–3395 (1985).
28. Miyashita, S. Magnetic properties of ising-like heisenberg antiferromagnets on the triangular lattice. *J. Phys. Soc. Jpn.* **55**, 3605–3617 (1986).
29. Sheng, Q. & Henley, C. L. Ordering due to disorder in a triangular heisenberg antiferromagnet with exchange anisotropy. *J. Physics: Condens. Matter* **4**, 2937 (1992).
30. Metcalf, B. Phase diagram of a nearest neighbor triangular antiferromagnet in an external field. *Phys. Lett. A* **45**, 1–2 (1973).
31. Schick, M., Walker, J. & Wortis, M. Antiferromagnetic triangular ising model. *Phys. Lett. A* **58**, 479–480 (1976).
32. Saito, Y. & Igeta, K. Antiferromagnetic ising model on a triangular lattice. *J. Phys. Soc. Jpn.* **53**, 3060–3069 (1984).
33. Kinzel, W. & Schick, M. Phenomenological scaling approach to the triangular ising antiferromagnet. *Phys. Rev. B* **23**, 3435 (1981).
34. Noh, J. D. & Kim, D. Phase boundary and universality of the triangular lattice antiferromagnetic ising model. *Int. J. Mod. Phys. B* **6**, 2913–2924 (1992).
35. Wu, F.-Y. The Potts model. *Rev. modern physics* **54**, 235 (1982).
36. Collins, M. & Petrenko, O. Review/synthèse: triangular antiferromagnets. *Can. journal physics* **75**, 605–655 (1997).
37. Gao, B. *et al.* Diffusive excitonic bands from frustrated triangular sublattice in a singlet-ground-state system. *Nat. communications* **14**, 2051 (2023).

38. Tennant, D., Perring, T., Cowley, R. & Nagler, S. Unbound spinons in the $s = 1/2$ antiferromagnetic chain KCuF_3 . *Phys. review letters* **70**, 4003 (1993).
39. Lake, B., Tennant, D. A., Frost, C. D. & Nagler, S. E. Quantum criticality and universal scaling of a quantum antiferromagnet. *Nat. materials* **4**, 329–334 (2005).
40. Lake, B. *et al.* Multispinon continua at zero and finite temperature in a near-ideal heisenberg chain. *Phys. Rev. Lett.* **111**, 137205 (2013).
41. Scheie, A. *et al.* Detection of kardar–parisi–zhang hydrodynamics in a quantum heisenberg spin-1/2 chain. *Nat. Phys.* **17**, 726–730 (2021).
42. Zhu, M. *et al.* Continuum excitations in a spin-supersolid on a triangular lattice. *arXiv preprint arXiv:2401.16581* (2024).
43. Cao, H. *et al.* Demand, a dimensional extreme magnetic neutron diffractometer at the high flux isotope reactor. *Crystals* **9**, 5 (2018).
44. Tagay, Z., Romero III, R. & Armitage, N. High-precision measurements of terahertz polarization states with a fiber coupled time-domain thz spectrometer. *arXiv preprint arXiv:2312.13276* (2023).

Acknowledgements

We gratefully acknowledge valuable discussions with Wei Li, Yuan Gao, Andreas Läuchli, Cristian Batista, Roderich Moessner, Changle Liu, Shu Zhang, and Oleg Tchernyshyov. This work was supported as part of the Institute for Quantum Matter, an Energy Frontier Research Center funded by the U.S. Department of Energy, Office of Science, Basic Energy Sciences under Award No. DE-SC0019331. C.B. was supported by the Gordon and Betty Moore Foundation EPIQS program under GBMF9456. Y.H. and H.C. were supported by the U.S. Department of Energy, Office of Basic Energy Sciences, Early Career Research Program Award KC0402020. A portion of this work was performed at the National High Magnetic Field Laboratory, which is supported by the National Science Foundation Cooperative Agreement No. DMR-2128556*, the U.S. Department of Energy, and the State of Florida. This research used resources at the High Flux Isotope Reactor and Spallation Neutron Source, a DOE Office of Science User Facility operated by Oak Ridge National Laboratory.

Author contributions

T.C., R.Z., and C.B. initiated this work. A.G., X.X., and R.C. prepared the samples. T.C., Y.H., H.C., and B.W. carried out neutron scattering experiments. A.G., E.C., M.J., and M.L. measured high-field magnetization. L.S., Z.T., and N.P.A. performed THz measurements. T.C., A.G., J.Z., L.C., and C.B. wrote the manuscript with input from all coauthors.

Competing interests

The authors declare no competing interests.

Figures

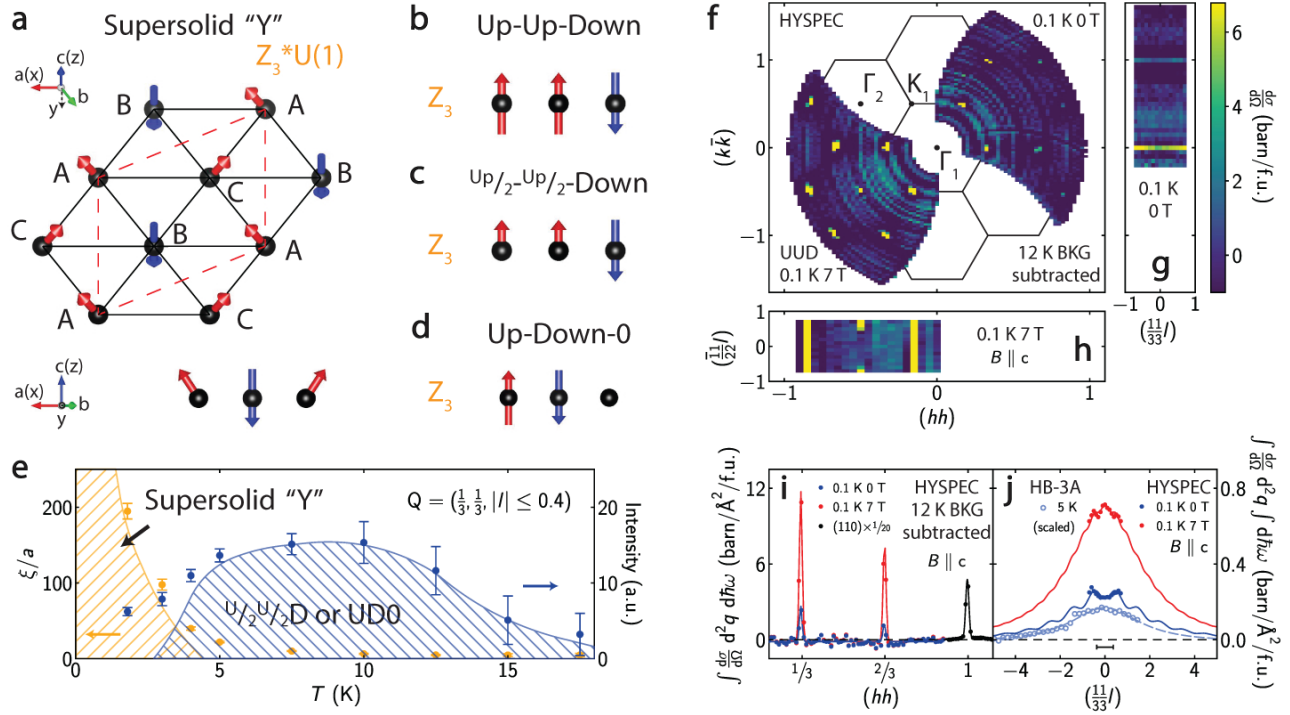


Figure 1. Three-sublattice magnetic orders and elastic scattering of KCSO. (a-d) Diagram of the supersolid "Y", UUD, $U/2U/2D$, and UD0 order on a triangular lattice with associated broken symmetries. A, B, and C are three sublattices. Red dashed lines indicate the $\sqrt{3} \times \sqrt{3}$ magnetic unit cell. (e) Correlation length and integrated intensity determined from the $(\frac{1}{3}\frac{1}{3})$ elastic scattering as functions of temperature measured on HYSPEC with incident energy of 3.8 meV in zero field. See Supplementary Information for details. (f-h) Elastic magnetic scattering as a function of momentum measured at 0.1 K in 0 T and 7 T magnetic field along the c -axis. (i,j) Momentum dependence of the $(\frac{1}{3}\frac{1}{3})$ elastic magnetic excitation along the (hh) and l directions. Scaled cuts and FWHM of the (110) nuclear peak show instrumental resolutions along two directions. Elastic scattering measured at 5 K is scaled according to the temperature dependence of the intensity at $(\frac{1}{3}\frac{1}{3}0)$. The red line is normalized to the UUD order with saturation moment $3.90 \mu_B/\text{Co}$. The blue and light blue lines correspond to the $U/2U/2D$ order with $3.09 \mu_B/\text{Co}$ and $2.51 \mu_B/\text{Co}$, respectively. Elastic scattering in panels (f-j) measured on HYSPEC is obtained with $E_i = 9.0$ meV. Statistical errors are within the symbols.

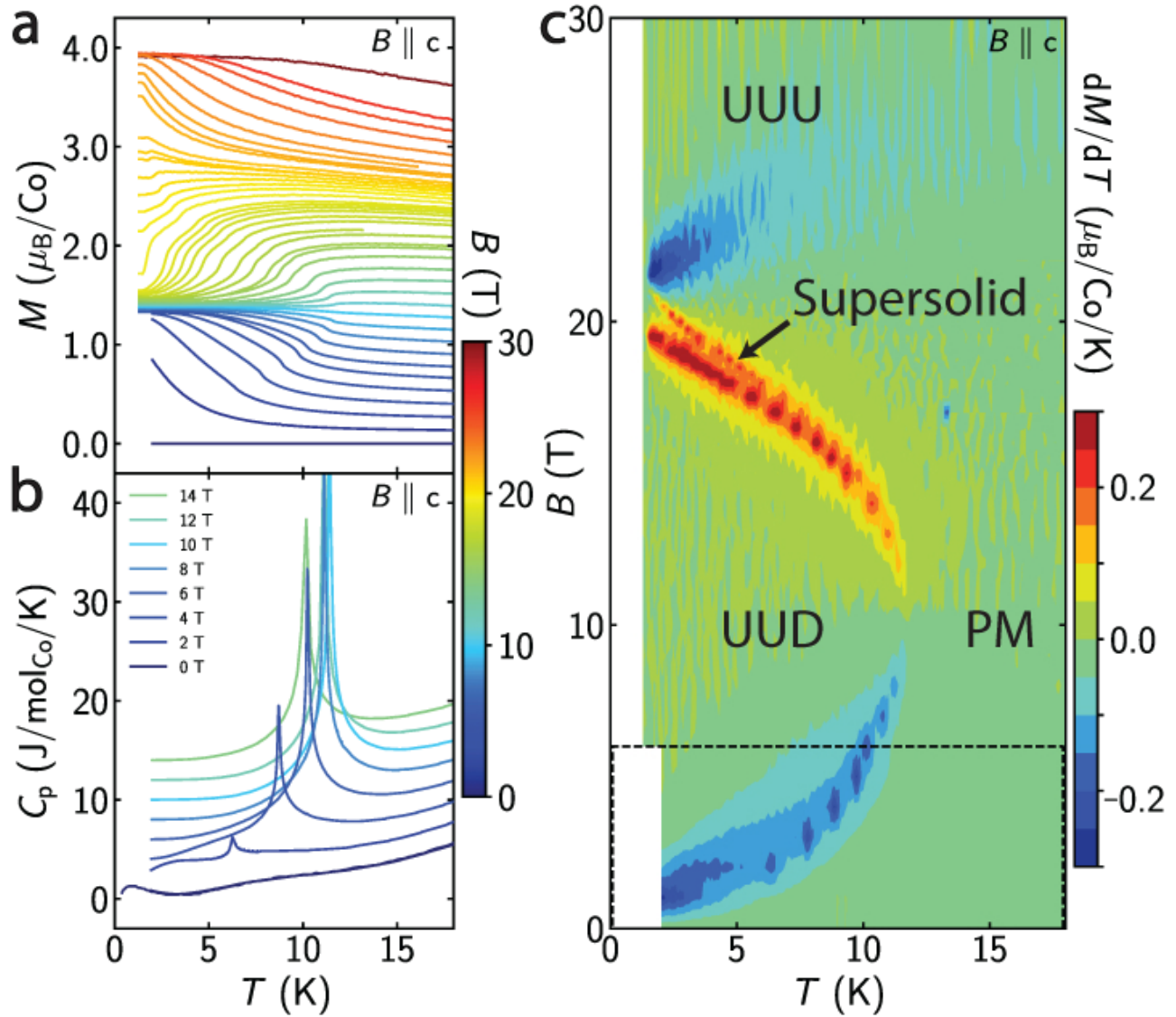


Figure 2. Temperature dependence of magnetization and specific heat, and phase diagram of KCSO. (a) Magnetization versus temperature at various c-axis-oriented fields up to 30 T. (b) Specific heat as a function of temperature, systematically shifted in the field ($+B$ (T)). Specific heat in zero field from Ref.¹⁰ is over-plotted on top of measured data with permission. (c) Contour plot of differential susceptibility, dM/dT , versus magnetic field and temperature. UUU, UUD, and PM represent Up-Up-Up (field-polarized), Up-Up-Down, and paramagnetic phases, respectively. Dashed lines show the low-field region further examined in Fig. 3.

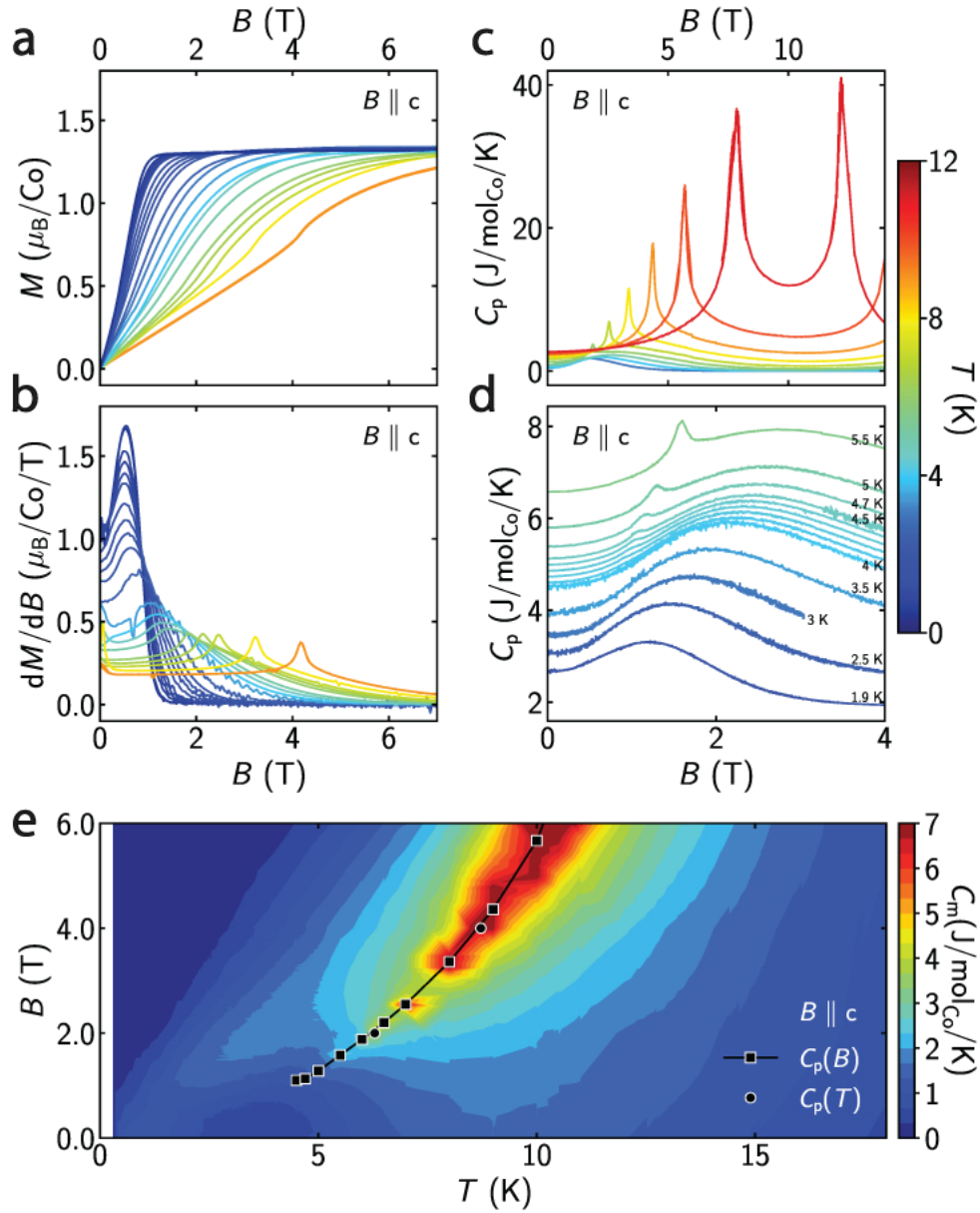


Figure 3. Magnetic field dependence of magnetization and specific heat, and phase diagram of KCSO. (a) Magnetization versus c-axis-oriented field at various temperatures down to 0.5 K. (b) Derivative of magnetization, dM/dB , as a function of field. (c) Specific heat versus field up to 14 T at various temperatures. (d) Low-field specific heat as a function of the field around 4.5 K. Data are systematically shifted in temperature ($+T$ (K)) to show the onset of a sharp transition. (e) Contour plot of magnetic specific heat C_m versus field and temperature. The field-independent lattice contribution to specific heat was fitted by the Debye model and subtracted from C_p . The second-order phase transition defined by peak positions in C_p versus temperatures (Fig. 2b) and field (Fig. 3c, d) appears to terminate at $(T, B) = (4.5 \text{ K}, 1.1 \text{ T})$. Data in the temperature window of 0.3 K to 1.9 K are reproduced from Ref. ¹⁰ with permission.

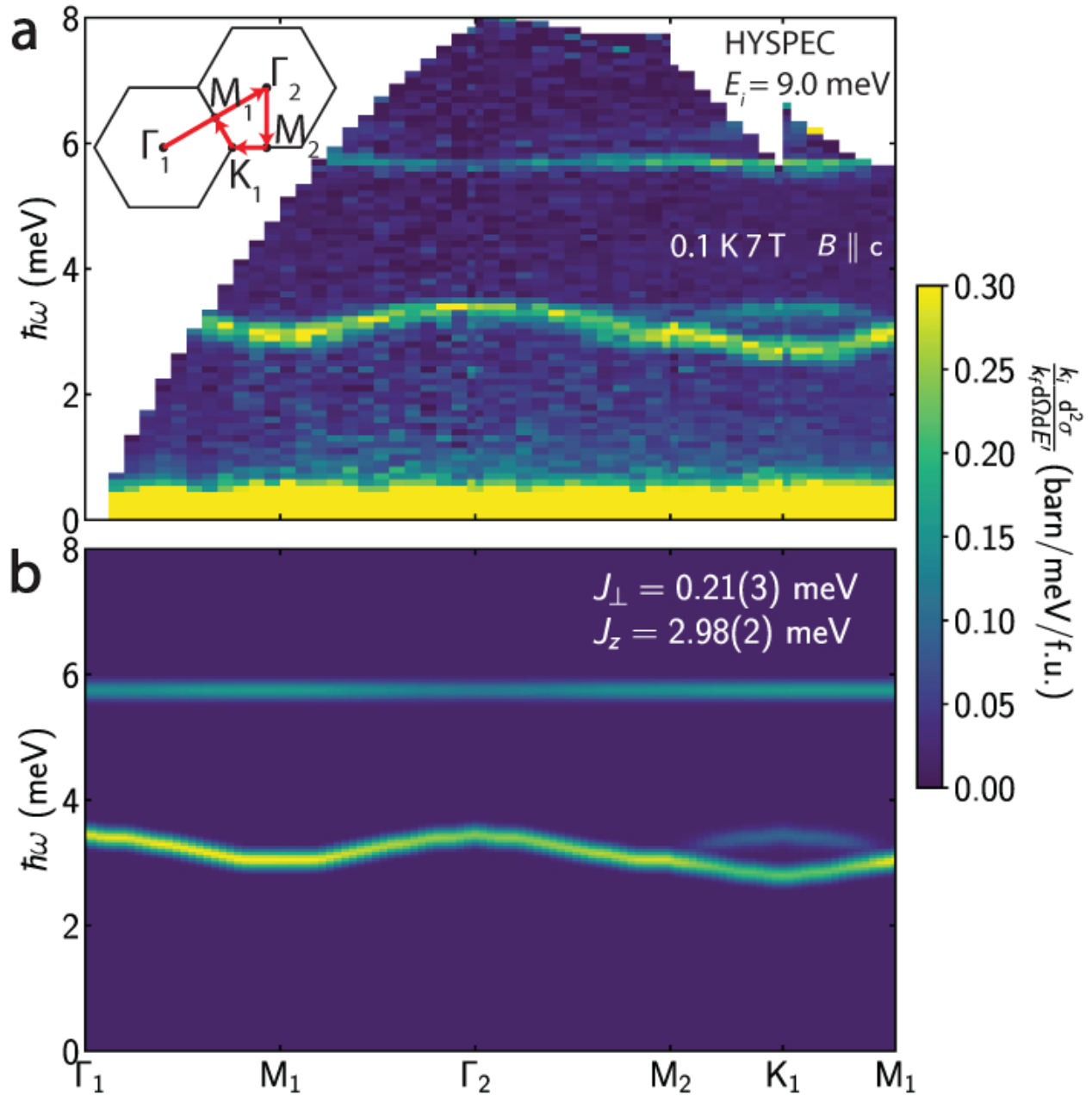


Figure 4. Coherent spin waves of KCSO in the UUD phase. (a) Energy-momentum (E - Q) spectrum along high-symmetry directions in a 7 T magnetic field along the c -axis at 0.1 K. The red path is illustrated in the diagram of the Brillouin zone. The data are averaged along the l direction. (b) Spin-wave excitations with fine pixel size simulated by linear spin-wave theory calculations along high-symmetry directions in a 7 T field. The parameters J_{\perp} and J_z are obtained by pixel-to-pixel fitting of the measured spectrum in panel (a) against the spin-Hamiltonian in Equation 1.

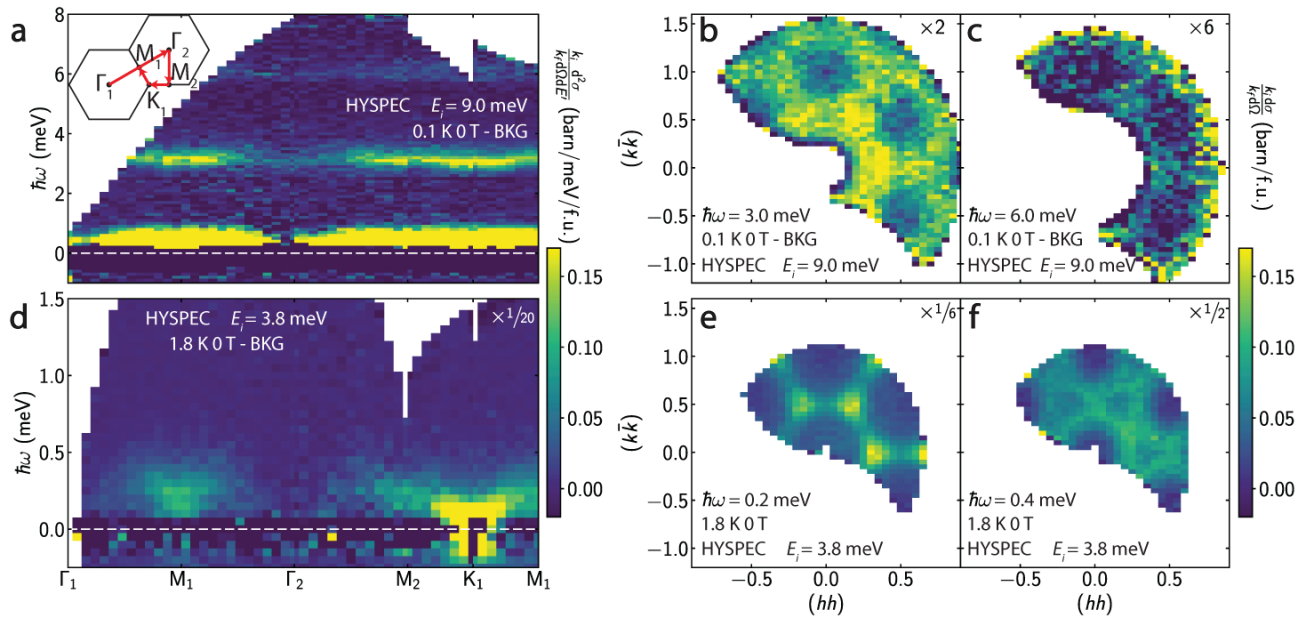


Figure 5. Magnetic excitations of KCSO in zero field. (a) E - Q spectrum along high-symmetry directions in zero field at 0.1 K with $E_i = 9.0$ meV. Scattering in the 7 T field and a constant are subtracted as background below and above 2.5 meV, respectively. (b,c) Magnetic scattering as a function of momentum and energy in the (hk) plane. A constant background is subtracted. (d) E - Q spectrum along high-symmetry directions at 1.8 K with $E_i = 3.8$ meV. Scattering in the 4 T field is subtracted. Scattering in the 4 T field is subtracted as background. (e,f) Magnetic scattering as a function of momentum and energy in the (hk) plane. All data shown are averaged along the l direction.